Type of contribution:
Editorial
▶ Research Paper
Case Study
Review Paper
Scientific Data
Report of Tech. Application

e-issn. 2798-5245
Mechanical Engineering for Society and Industry
Vol. 6, No. 2 (2026) pp 362-382
https://doi.org/10.31603/mesi.16083

Electromechanical and CFD-coupled analysis of deflector-guided savonius pico-hydro turbine with quarter-circular blade rotors

Rinasa Agistya Anugrah[1]*, Sudarja[2], Yosef Budiman[3], Muhammad Yusri Ilyas[3]

[1] Department of Automotive Engineering Technology, Universitas Muhammadiyah Yogyakarta, Bantul 55183, **Indonesia**
[2] Department of Mechanical Engineering, Universitas Muhammadiyah Yogyakarta, Bantul 55183, **Indonesia**
[3] PT Sahla Inovatif Teknik, Sleman 55581, **Indonesia**
✉ rinasaanugrah@umy.ac.id

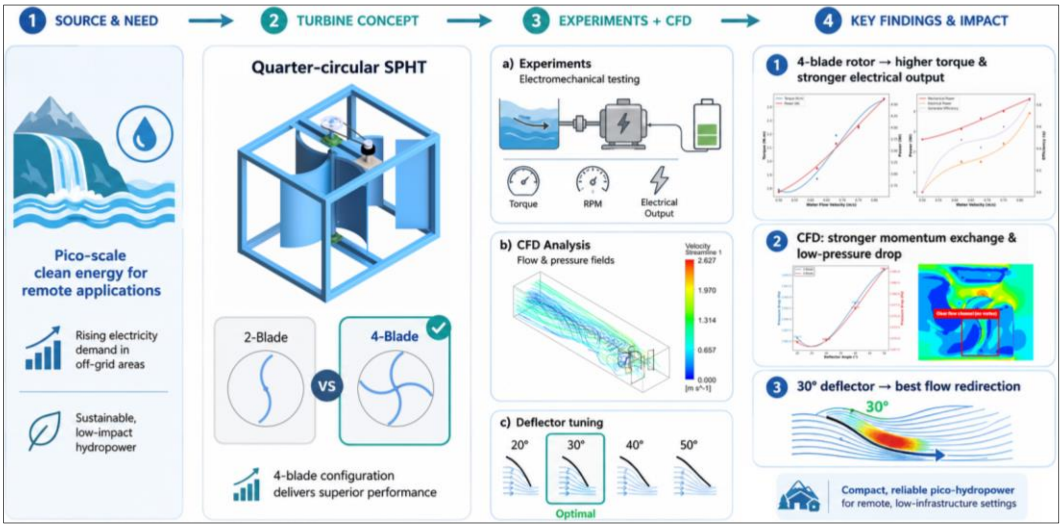

Highlights:

- Electrical output and generator efficiency of SPHT were quantified.
- Experiments were coupled with CFD to explain rotor flow behavior.
- The four-blade rotor produced higher torque than the two-blade rotor.
- Four blades improved electrical response under realistic loading.
- A 30° deflector gave the most effective flow redirection.

Article info
Submitted: 2026-01-29
Revised: 2026-06-02
Accepted: 2026-07-13

Publisher
Universitas Muhammadiyah Magelang

Abstract

Global electricity demand continues to rise, increasing dependence on fossil fuels and accelerating greenhouse gas emissions that contribute to climate instability. Small-scale hydropower offers a clean alternative, particularly for distributed and space-constrained applications where conventional hydropower systems are difficult to implement. Among available concepts, the Savonius Pico-Hydro Turbine (SPHT) is attractive because of its simple structure, low production cost, and good self-starting capability. However, previous studies have mainly focused on mechanical performance, while the combined evaluation of mechanical response, electrical output, generator efficiency, and hydrodynamic flow behavior remains limited. The novelty of this study lies in the use of a quarter-circular blade profile instead of the commonly used semi-circular Savonius blade, combined with experimental electromechanical testing, CFD-based flow visualization, and deflector-angle variation. Two- and four-blade SPHT configurations were examined under realistic loading conditions, while CFD simulation was employed to clarify velocity distribution, pressure loading, momentum exchange, and deflector-guided flow patterns. The results showed that the four-blade rotor produced higher torque and a stronger electrical response than the two-blade rotor. CFD contour analysis supported these findings by showing stronger momentum exchange and more distributed pressure loading around the higher-solidity rotor. The deflector investigation further indicated that a 30° deflector angle provided the most effective flow redirection and pressure distribution among the evaluated cases. Overall, the proposed experimental and numerical framework provides a practical basis for optimizing quarter-circular SPHT design through blade configuration selection and deflector-angle tuning, supporting compact and reliable pico-scale clean energy generation for remote and low-infrastructure applications.

Keywords: CFD simulation; Deflector angle; Pico-hydro turbine; Savonius blade; Water flow

1. Introduction

In the current era, global energy consumption is accelerating by 4.3%, recorded at 1080 TWh in 2024 [1]. To meet this demand, many countries are pushing to utilize non-renewable energy sources, such as oil, gas, and coal, due to their practicality [2], thereby depleting reserves [3]. On the other hand, these actions cause an unstable climate, increasing greenhouse gas (GHG) emissions [4], indicated by rising earth temperatures and sea levels [5], which have a significant impact on human life and disrupt the balance of the global ecosystem [6], [7]. To support environmental sustainability, many countries have developed alternative energy sources to meet increasing electricity demand [8]. According to this view, hydroelectric power is a promising renewable energy source emerging as an alternative to wind power [9], primarily because it does not emit pollutants into the atmosphere [10].

There are many ways to describe hydroelectric power; however, the most widely accepted approach is the Savonius Pico-Hydro Turbine (SPHT). With its simple design, low production cost, and excellent starting ability [11], numerous studies have been conducted to measure its mechanical performance. Regarding blade design, Sarma *et al*. [12] developed a dual-stage blade configuration to improve hydrokinetic performance under low-flow stream conditions. In another mechanical investigation, Basumatary *et al*. [13] conducted a numerical study to determine the optimum deflector design for a two-bladed Savonius turbine. Further extending the mechanical performance analysis, Nath *et al*. [14] evaluated a modified Savonius hydrokinetic turbine (MSHT) with straight and curved winglets by examining the coefficient of power (C_p) and tip-speed ratio (TSR), and optimized the winglet configuration to maximize mechanical output.

Although previous studies have contributed to the development of Savonius hydrokinetic turbines through blade modification, deflector optimization, and mechanical performance analysis, several research gaps remain. Most existing Savonius turbine studies still employ conventional semi-circular blade profiles, while the use of a quarter-circular blade profile for Savonius Pico-Hydro Turbine applications has received limited attention [15]. In addition, previous investigations have commonly emphasized mechanical indicators such as torque, power coefficient, and tip-speed ratio, whereas the electrical output characteristics and generator efficiency under practical loading conditions are still rarely discussed. Another limitation is that many Savonius turbine studies, particularly those adapted from wind turbine research, are still conducted without incorporating a deflector to guide the incoming flow toward the advancing blade. As a result, the potential contribution of a deflector in improving flow utilization and enhancing the performance of a quarter-circular SPHT rotor remains insufficiently explored.

Therefore, to address these gaps, the novelty of the present study lies in developing and evaluating a Savonius Pico-Hydro Turbine with a quarter-circular blade profile instead of the commonly used semi-circular blade. Furthermore, this study combines mechanical and electrical experiments with Computational Fluid Dynamics (CFD) simulation to examine turbine performance and visualize the associated flow behavior [16]. Extending the blade-number examination previously reported by Anugrah *et al*. [17], two- and four-blade SPHT rotors were selected as the main configurations, while the three-blade configuration was excluded because it may cause mass imbalance, significant vibration, and poor starting behavior [18], [19], [20], which can reduce both mechanical and electrical output. In addition to the novelty aspect, variations in deflector angle were applied to evaluate how flow guidance influence turbine performance under specific loading conditions.

Accordingly, this study aims to: 1) compare the mechanical performance, including torque and power, and electrical performance, including voltage, current, and power, of two- and four-blade SPHT rotors; 2) integrate experimental results with CFD simulation to clarify the velocity and pressure distributions around the rotor; and 3) determine the optimum deflector angle for enhancing flow redirection. Through this integrated approach, the study links blade geometry, input velocity, deflector-guided flow, mechanical output, electrical response, and generator efficiency in a single performance assessment.

Eventually, this research builds a clear understanding of how the SPHT can contribute to more efficient, practical small-scale generators, offering a new, more compact solution for generating clean energy in space-constrained or distributed applications. By systematically comparing the three mentioned aspects and validating performance under real river conditions with a stepper-motor generator and defined electrical loading, the study links rotor geometry and operating kinematics directly to measurable power output at the pico-energy scale. The findings therefore provide an engineering basis for optimizing SPHT design toward reliable deployment in remote or low-infrastructure locations, where simple construction, ease of maintenance, and consistent energy harvesting are essential. In this way, the proposed system supports broader renewable-energy adoption by enabling localized, low-cost generations that complement larger centralized power systems.

2. Methods

2.1. SPHT Design Overview

Before proceeding to a comprehensive analysis, the SPHT design was developed to provide clear information on the generator's operation. In this study, the main rotor consists of curved blade surfaces designed with a quarter-circular profile and mounted concentrically around a vertical rotor shaft. This geometry forms distinct concave driving surfaces and convex returning surfaces during operation, enabling the incoming water flow to generate pressure-driven torque on the rotor. To ensure comparability between test cases, the rotor configuration was defined as either two-blade or four-blade while maintaining the same quarter-circular blade profile. This approach allows the effect of blade count on swept area, flow interaction, and torque generation to be evaluated without interference from unintended changes in blade geometry.

By maintaining the same blade profile, the entire assembly exhibited in **Figure 1** also demonstrates how the rotor was integrated into the mechanical or electrical experiment setup. The rotor shaft was supported by a bearing mounted on the upper frame to minimize frictional losses and to maintain stable rotation with minimal radial misalignment. In addition, a transmission pulley mounted on the shaft enabled mechanical or electrical coupling to the loading and instrumentation system. To reduce negative torque and increase net rotational output, a deflector with a 30° angle was installed near the rotor to direct the inflow onto the advancing blade surface and to partially shield the returning side [21]. All components were embedded in a rigid frame to ensure that boundary conditions remain constant throughout the experimental runs. In this research, a stepper motor was employed as the generator, selected for its practicality and availability for low-speed rotational systems, enabling conversion of mechanical rotation into electrical energy suitable for pico-scale generation with power capacity below 5 kW [22].

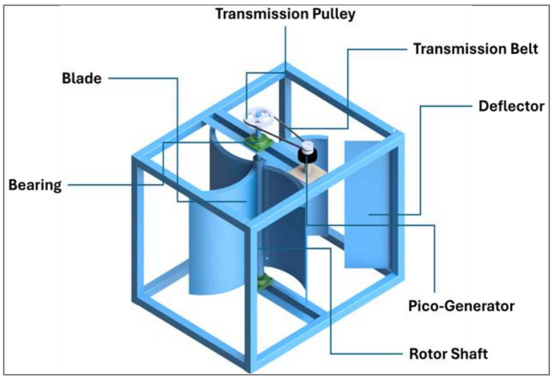

Figure 1. SPHT full assembly

2.2. Blades Configuration

Building on the SPHT assembly described in the previous section, where the rotor, shaft–bearing support, transmission pulley, and stepper-motor generator were integrated into a single testable unit, this subsection details the blade configurations used to evaluate the effect of rotor solidity on performance. As shown in **Figure 2**, two rotor layouts were examined, namely two-blade and four-blade configurations, both adopting the same quarter-circular curved blade profile. The geometric reference lines in **Figure 2** define the rotor radius R, the quarter-circular (90°) blade construction, and the angular positioning of the blades about the central shaft. In the two-blade configuration, the blades were arranged opposite each other with 180° separation, forming a balanced rotor layout. In the four-blade configuration, four quarter-circular (90°) blades were distributed around the same shaft axis with uniform angular spacing to increase rotor solidity while maintaining geometric symmetry. The 45° reference line was included to clarify the blade orientation and angular construction relative to the rotor centerline. By maintaining the same blade profile and shaft axis in both configurations, the influence of blade count on flow interaction, pressure-driven torque, and rotational response could be evaluated without unintended changes in blade geometry.

To isolate the influence of blade numbers, all dimensional features were held constant across configurations, as depicted in Table 1. The rotor utilized a 47.60 mm shaft diameter and an overall rotor diameter of 680 mm, while each blade was manufactured with a 220.72 mm length and a defined 90.36° curvature angle, representing the intended blade wrap and flow-capturing geometry. In addition, the tip surface area (50,000 mm²) was kept constant to preserve the effective exposed area at the outer radius, where the tangential velocity was highest and contributed strongly to aerodynamic torque. With these fixed dimensions, the comparison between two- and four-blade configurations reflected changes in flow interaction rather than differences in blade size or rotor radius.

Table 1. Dimensional features of SPHT blades

Part Features	Value	Unit
Number of blades	2/4	-
Shaft diameter	47.60	mm
Rotor diameter	680	mm
Tip surface area	50,000	mm²
Blade diameter	441.45	mm
Blade curvature angle	90.36	degree (°)
Blade length	220.72	mm

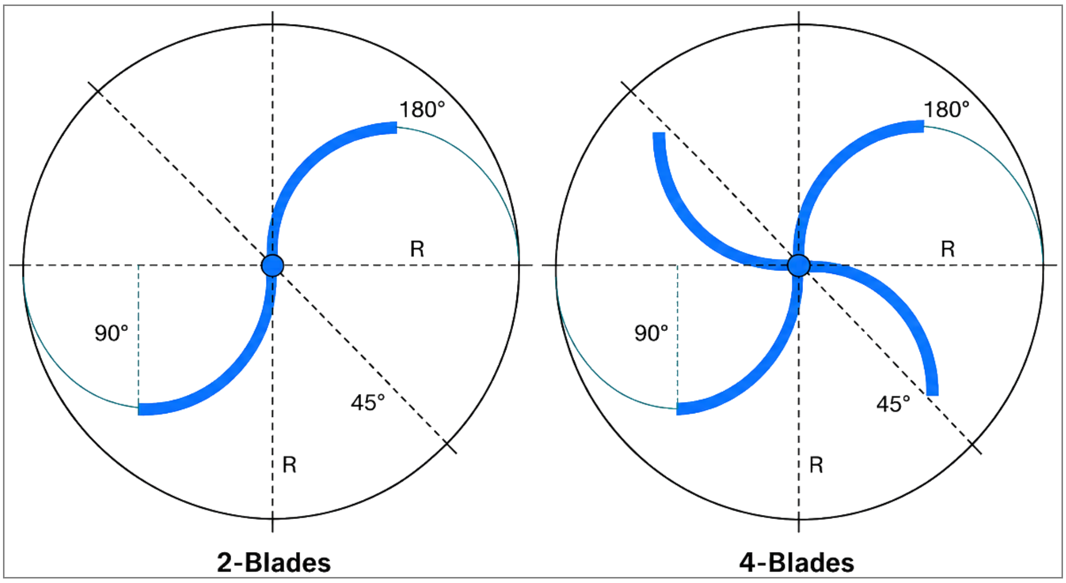

Figure 2. SPHT blade configurations

2.3. Research Procedure

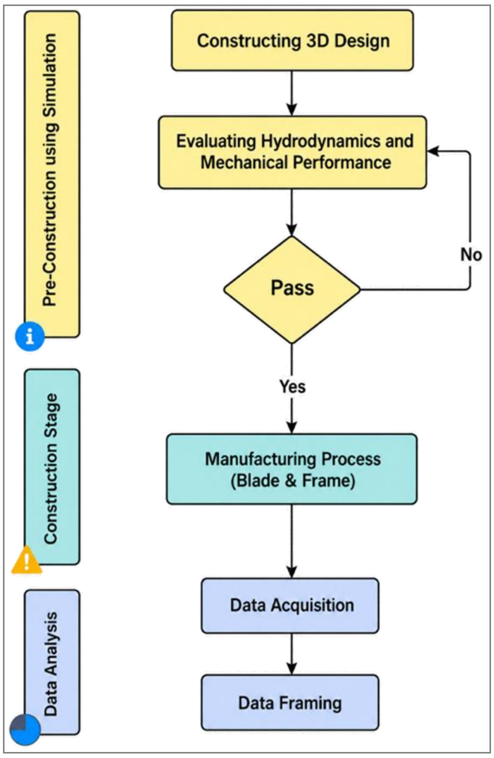

Figure 3. Research procedure

The research procedure was arranged to clearly separate the experimental and numerical outputs used in this study, as shown in Figure 3. The procedure began with the construction of the three-dimensional SPHT model, followed by a pre-construction simulation stage to evaluate hydrodynamic behavior and mechanical feasibility before manufacturing. If the initial design did not meet the expected performance criteria, the design was revised and re-evaluated. Once the design passed this stage, the blade and frame were manufactured, and the prototype was prepared for experimental testing.

In this study, all numerical performance data related to rotor operation were obtained from experimental measurements. These data included rotational speed, torque, mechanical power, voltage, current, electrical power, and generator efficiency. Therefore, the mechanical and electrical performance comparisons between the two-blade and four-blade SPHT configurations were based on recorded experimental data under the defined operating conditions. The experimental stage was followed by data acquisition and data framing to organize the measured parameters for performance analysis.

Meanwhile, the CFD simulation was not used as the primary source of numerical electromechanical performance data. Instead, it was used as a supporting numerical tool to visualize the hydrodynamic flow characteristics around the rotor and deflector. The CFD results were mainly presented in the form of velocity and pressure contours to explain flow acceleration, pressure distribution, recirculation, and wake formation. In particular, CFD was used to compare the flow-guiding effect of different deflector angles and to identify the most favorable deflector configuration. Thus, the experimental results provided the quantitative mechanical and electrical performance data, while the CFD analysis provided flow-visualization evidence to support the interpretation of rotor behavior and deflector-angle optimization.

2.4. Experimental Setup

Following the defined rotor geometry and blade configurations, the experimental setup was arranged to quantify the rotor kinematics under controlled inflow conditions, as illustrated in Figure 4. The rotor was exposed to an incoming water stream of velocity (U), and its motion was described using the angular position (θ) and angular velocity ($\omega = d\theta/dt$) about the shaft axis. The characteristic rotor size was represented by the radius (R) (from shaft center to blade tip), while the geometric reference dimensions of the blade and shaft diameter were denoted by d and a, respectively, defining the effective projected length and local offset at the tip region. These parameters were consistently employed throughout testing to relate the measured rotational response (RPM/ω) to the imposed water speed and to establish the basis for subsequent performance metrics, such as tip-speed ratio and torque–speed behavior.

Building on the kinematic definitions in Figure 4, the experimental campaign was then conducted under real environmental conditions to capture the practical operating behavior of the SPHT system. As portrayed in Figure 5, the assembled turbine was deployed in a river segment characterized by low waves and relatively unsteady surface flow, allowing the rotor to operate under natural hydrodynamic forcing while maintaining stable support from the frame. The rotor output was coupled to the stepper-motor generator, and the electrical response was monitored using a multimeter for voltage or current measurement, while the external electrical load was predefined to represent pico-scale energy extraction conditions. This arrangement enabled direct evaluation of how the rotor's rotational response translated into measurable electrical output under field-relevant flow conditions, while maintaining consistent loading and measurement procedures across blade configurations.

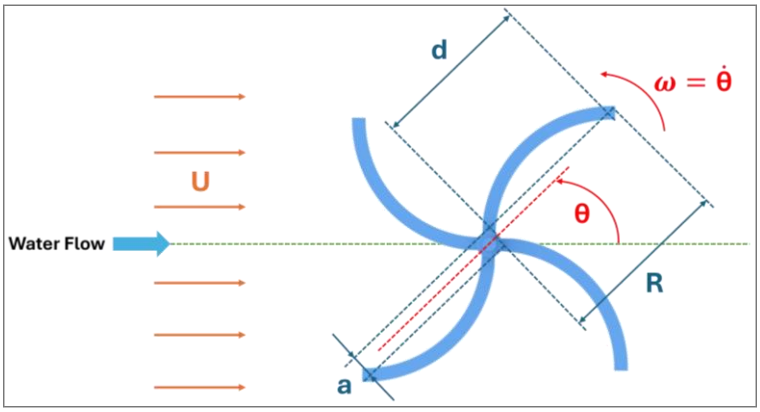

Figure 4. Kinematics profile of SPHT's blade

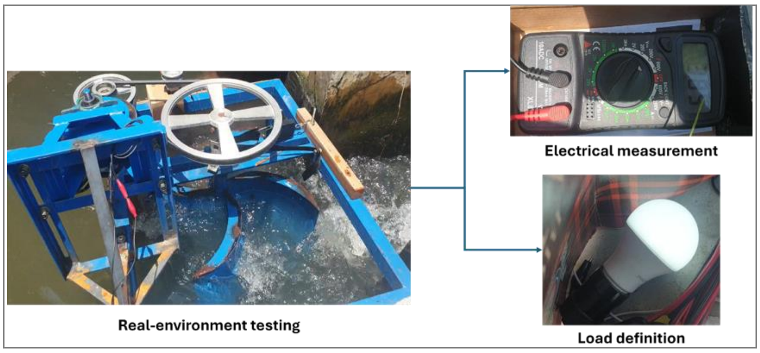

Figure 5. SPHT testing in rivers with low waves

2.5. SPHT Performance Measurement

To quantify the turbines' performance, several key parameters were considered: torque output, torque coefficient, power output, power coefficient, and tip-speed ratio. These parameters served to assess overall performance and make comparisons with alternative turbine configurations [23]. Torque (τ) was determined by multiplying centrifugal force on the blades by the blade length as the rotor radius, as depicted in Eq. (1).

$$\tau = F \times r \tag{1}$$

F denotes the tangential force on the blades and r indicates the rotor radius. Power (P) was obtained by multiplying the torque by the turbine's angular speed in Eq. (2), while ω signifies the rotational (angular) velocity of the rotor.

$$P = \tau \times \omega \tag{2}$$

Moreover, the tip-speed ratio (λ) is defined as the blade-tip speed divided by the free-stream wind speed, as demonstrated in Eq. (3).

$$\lambda = \frac{\omega D}{2V} \tag{3}$$

ω implies the rotor's angular speed, D represents the rotor diameter, and V depicts the wind velocity.

Furthermore, in Eq. (4), the power coefficient (C_p) is defined as the proportion between the wind's power and the measured kinetic power, included in the airflow inlet.

$$C_p = C_t \, x \, \lambda = \frac{P}{\left(\frac{1}{2}\rho DHV^3\right)} \tag{4}$$

In addition, the torque coefficient (C_t) is a dimensionless metric defined as the rotor's delivered torque divided by the torque available from the wind acting on the swept area, as formulated in Eq. (5). It indicates how effectively the turbine converts aerodynamic torque into mechanical output, enabling performance comparisons across different sizes, tip-speed ratios, and operating conditions.

$$C_t = \frac{T}{\left(\frac{1}{4}\rho D^2 HV^2\right)} \tag{5}$$

where, T denotes torque, ρ indicates the air density, D represents the rotor diameter, H signifies the rotor height, and U depicts the free-stream wind speed.

In an electrical context, the generator rotor obtains mechanical power from the turbine shaft and converts it into electrical power. The generator efficiency (η_g) depends upon the turbine's shaft power and electrical output power. As formulated by Safdar *et al*. [24], the efficiency of electrical power can be calculated in Eq. (6).

$$\eta_g = \frac{W_{elec}}{W_S} \tag{6}$$

The electrical power from the generator (W_{elec}) and shaft power of the turbine (W_S) can be determined by Eq. (7) and Eq. (8), respectively.

$$W_{elec} = VI \tag{7}$$

$$W_S = \frac{2\pi\omega\tau}{60} \tag{8}$$

Eventually, VI is the voltage and current across the generator terminal.

2.6. Data Acquisition (DAQ) Technique

To capture accurate data during measurement, data acquisition is essential for quantifying SPHT performance reliably, particularly when comparing different blade configurations under variable flow conditions. In this study, torque was measured with a load cell, and rotational speed (RPM) was captured with an infrared (IR) sensor. The load cell provided high sensitivity to small force changes and enabled stable, repeatable torque estimation when combined with a known lever arm, reducing measurement noise that typically arises from mechanical oscillations in field testing. In parallel, the IR sensor enabled non-contact RPM detection via pulse counting, improving precision at both low and fluctuating rotational speeds while minimizing disturbance to the rotor dynamics. Together, these sensors provided a synchronized, high-resolution dataset, supporting higher accuracy and repeatability in calculating derived metrics, such as power and tip-speed ratio.

An additional justification for this approach is that manual force-based methods, such as using a spring scale as demonstrated by Sahim *et al*. [25], are generally not recommended for rigorous performance characterization. Spring-scale measurements depend heavily on operator judgment in reading a fluctuating scale, creating subjectivity and increasing the likelihood of human error, especially under unsteady flow where force varies continuously. Moreover, the method typically provides limited data resolution because readings are taken at discrete times rather than continuously, making it difficult to capture transient behavior and compute reliable averages and uncertainty bounds. For these reasons, sensor-based DAQ is preferred to ensure consistent measurement quality and to enable objective comparison across experimental runs.

To implement the DAQ system, the sensors and peripherals were integrated according to the architecture displayed in **Figure 6**, with an Arduino Uno serving as the central microcontroller. The load cell signal was routed through an HX711 amplifier or ADC module before entering the Arduino for calibration and conversion into force, which was then utilized to compute torque based on the known moment arm. Rotor speed was detected using an optocoupler (RPM) sensor, which generated digital pulses that the Arduino counted to calculate RPM in real time. A push button was included as a user input to initiate or reset acquisition, while the processed values were displayed directly on a device LCD for immediate monitoring. For the electrical load interface, the Arduino controlled a ULN2003 driver module connected to the stepper motor, enabling stable interfacing and protection for the microcontroller I/O. All components were powered through a regulated power supply, ensuring consistent sensor readings and reliable data logging during field operation.

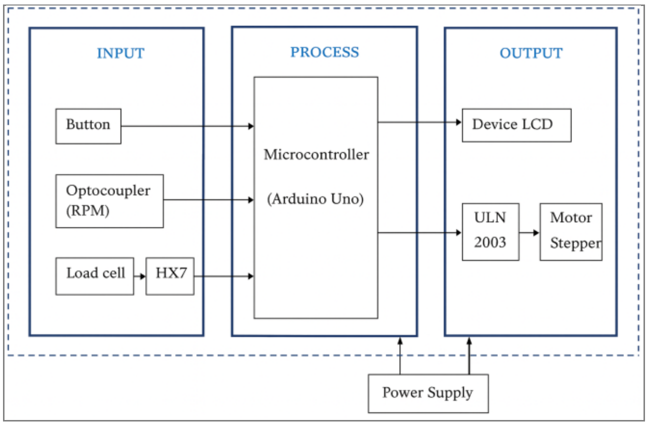

Figure 6. Block diagram of control system in SPHT [26]

2.7. Simulation Setup Through Computational Fluid Dynamics (CFD)

The flow simulations in ANSYS Fluent 2024 R1, a commercial CFD platform used to resolve aerodynamic behavior, were performed in this study. The governing equations utilized the incompressible Reynolds-averaged Navier–Stokes (RANS) equations, which govern the time-averaged conservation of mass and momentum for turbulent flows. A volume-of-fluid (VOF) formulation was adopted to capture the phase interface, while turbulence closure was provided by the standard RANS-based k–ω SST model. This modeling approach is supported by Anugrah *et al*. [27], who demonstrated its applicability in turbulent regimes where bulk rotation and swirl strongly affect flow development. The k–ω SST model is also suitable for predicting possible flow separation and recirculation within confined internal passages, as these phenomena require reliable near-wall boundary-layer resolution to accurately estimate pressure loss and velocity distribution [28]. These equations, together with appropriate boundary conditions and material properties for air, were discretized within boundary conditions and iteratively solved to obtain the velocity and pressure underpinning the performance analysis.

The CFD analysis was performed under steady-state conditions; therefore, all explicit time-dependent terms were omitted, and the governing equations were solved in a time-invariant form. The working fluid was considered incompressible and Newtonian, which is appropriate for the present low-speed water-flow simulation. With this assumption, the conservation of mass is expressed by the steady continuity in Eq. (9) as follows.

$$\frac{\partial u_i}{\partial x_i} = 0 \tag{9}$$

where, u_i is the mean velocity component in the x_i direction. After defining the continuity condition, the mean flow field was obtained from the steady Reynolds-averaged Navier-Stokes (RANS) momentum equation. The RANS formulation separates the mean-flow motion from the turbulent fluctuation contribution and can be written.

$$\frac{\partial}{\partial x_j}(\rho u_i u_j) = -\frac{\partial p}{\partial x_i} + \frac{\partial}{\partial x_j}\left[\mu\left(\frac{\partial u_i}{\partial x_j} + \frac{\partial u_j}{\partial x_i}\right)\right] - \frac{\partial}{\partial x_j}(\rho u_i' u_j') \tag{10}$$

In Eq. (10), ρ denotes the fluid density, p is the static pressure, μ is the dynamic viscosity, and $-\rho u_i{}'u_j{}'$ represents the Reynolds stress tensor caused by turbulent velocity fluctuations. Since the Reynolds stress introduces additional unknowns into the momentum equation, a turbulence closure model is required. In this study, the Reynolds stress was related to the mean velocity gradients using the Boussinesq eddy-viscosity approximation as provided in Eq. (11).

$$-\rho u_i{}'u_j{}' = \mu_t\left(\frac{\partial u_i}{\partial x_j}+\frac{\partial u_j}{\partial x_i}\right)-\frac{2}{3}\rho k\delta_{ij} \tag{11}$$

where, μ_t is the turbulent viscosity, k is the turbulent kinetic energy, and δ_{ij} is the Kronecker delta. This relationship allows the unresolved turbulent stresses to be represented through the resolved mean-flow gradients and the turbulent viscosity.

The turbulent viscosity was determined using the standard k-ω turbulence model. This model solves two additional transport equations: one for the turbulent kinetic energy k and another for the specific dissipation rate ω. The transport equation for k is expressed as shown in Eq. (12).

$$\frac{\partial}{\partial x_j}(\rho k u_j) = \frac{\partial}{\partial x_j}\left[\left(\mu+\frac{\mu_t}{\sigma_k}\right)\frac{\partial k}{\partial x_j}\right]+G_k-\beta\rho k\omega \tag{12}$$

The corresponding transport equation for ω is given by Eq. (13).

$$\frac{\partial}{\partial x_j}(\rho \omega u_j) = \frac{\partial}{\partial x_j}\left[\left(\mu+\frac{\mu_t}{\sigma_\omega}\right)\frac{\partial \omega}{\partial x_j}\right]+\alpha\frac{\omega}{k}G_k-\beta\rho\omega^2 \tag{13}$$

where, G_k is the production of turbulent kinetic energy, while α, β, β^*, σ_k, and σ_ω are empirical constants of the turbulence model. The turbulent viscosity was then calculated from k and ω as provided in Eq. (14).

$$\mu_t = \rho\frac{k}{\omega} \tag{14}$$

Furthermore, the production of turbulent kinetic energy was evaluated from the mean strain-rate magnitude as shown in Eq. (15).

$$G_k = \mu_t S^2 \tag{15}$$

where, S and S_{ij} are terms of the mean strain-rate tensor which provided in Eq. (16) and Eq. (17), respectively.

$$S = \sqrt{2S_{ij}S_{ij}} \tag{16}$$

$$S_{ij} = \frac{1}{2}\left(\frac{\partial u_i}{\partial x_j}+\frac{\partial u_j}{\partial x_i}\right) \tag{17}$$

Thus, the steady continuity equation, the steady RANS momentum equation, and the standard k-ω turbulence equations formed the governing mathematical framework for the CFD simulation. This formulation enabled the prediction of the mean velocity field, pressure distribution, turbulent shear effects, separation, recirculation, and wake development around the SPHT rotor and deflector. The governing model was subsequently implemented together with the computational domain, boundary conditions, mesh configuration, and numerical solution settings described in the following section.

To support and interpret the experimental findings, a computational fluid dynamics (CFD) approach was implemented to resolve the flow field and pressure loading around the SPHT rotor under controlled boundary conditions. As illustrated in **Figure 7**, the numerical domain was defined as a rectangular channel representing the test section, where the inlet boundary was prescribed as a uniform velocity inlet to replicate the imposed water-flow condition. In contrast, the opposite side was set as a pressure outlet to allow physically consistent discharge. The remaining surfaces were treated as no-slip walls, and a deflector was included upstream of the rotor to reproduce the guiding or shielding effect employed in the prototype. Within this domain, the rotor blades were positioned at the reference location and simulated to capture the resulting velocity distribution, recirculation zones, and pressure gradients that govern torque production, providing a mechanistic link between the measured performance and the underlying hydrodynamic behavior.

The boundary conditions illustrated in Figure 7 enabled accurate capture of the mechanical parameters influencing torque production. By integrating these parameters, the model establishes a mechanistic link between experimental performance and the system's underlying hydrodynamic behavior, thereby supporting the interpretation of the experimental findings.

Following the CFD boundary condition definition, the numerical model was configured using the domain and solver settings summarized in Table 2 to ensure stable and repeatable computation. The flow enclosure was constructed with overall dimensions of 9000 × 13799 × 6400 mm, representing the channel volume surrounding the SPHT rotor. The simulation was executed with a time scale factor of 0.5 and a profile update interval of 1, while solution convergence was targeted through 500 iterations for each inlet condition. Turbulence effects were modeled using the standard k–ω model, which provides a practical balance between numerical robustness and computational cost for flow problems involving separation, recirculation, and interaction with rotating bodies and obstacles such as the deflector. To support these solver settings and ensure that the important flow structures could be captured accurately, the computational domain was then discretized using a Poly-Hexcore mesh (see Figure 8) with an element size of 0.2 mm.

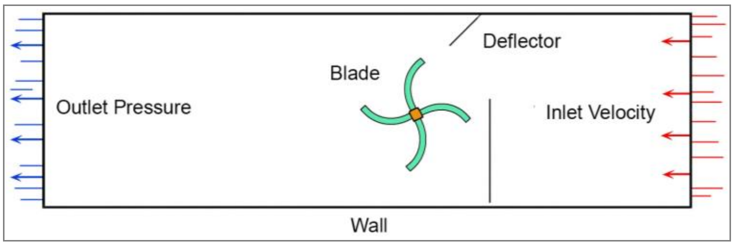

Figure 7. Boundary conditions of numerical simulation

Table 2. CFD domain setup

Parameters	Value
Mesh geometry	Poly-Hexcore
Element size (mm)	0.2
Enclosure dimension (mm)	9000 × 13799 × 6400
Time scale factor	0.5
Profile update interval	1
Number of iterations	500
Used turbulence model	k–ω SST

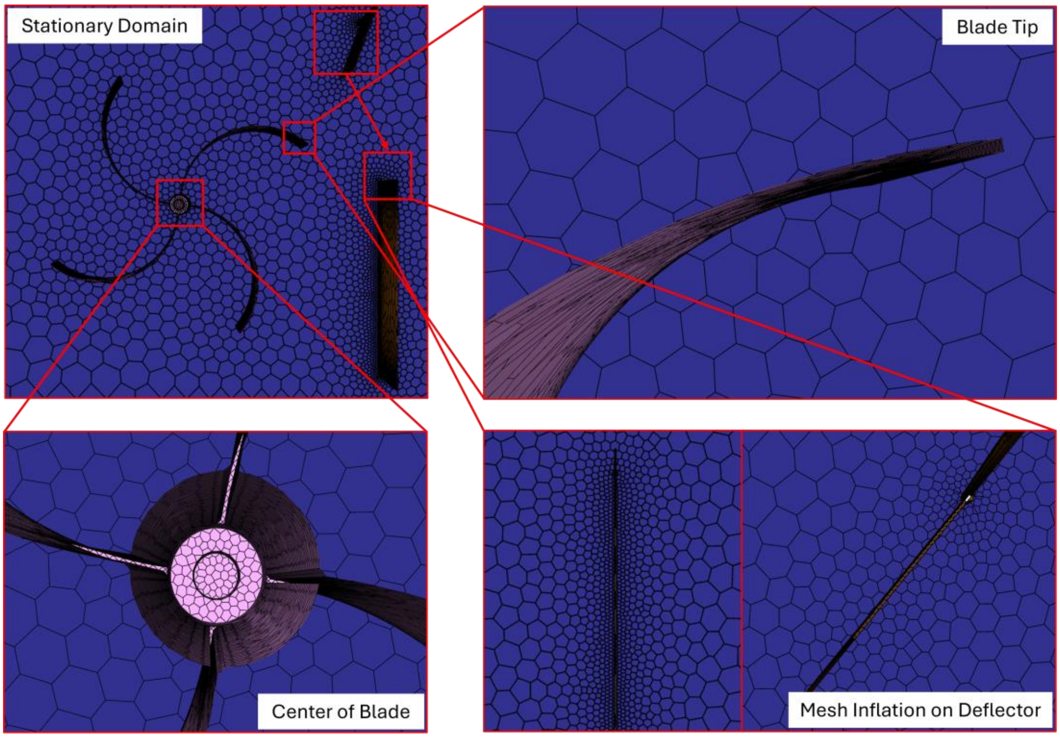

Figure 8. Poly-hexcore mesh configuration with local refinement around the SPHT rotor and deflector

The mesh refinement was mainly concentrated around the blade region, especially at the blade tip, blade center/root, and the deflector domain interface. These areas are critical because they are expected to contain strong velocity and pressure gradients, possible flow separation, and tip-vortex formation. Therefore, a finer mesh was required to capture the local flow behavior more accurately. Mesh inflation layers were also applied along the deflector surfaces to resolve the near-wall boundary layer and improve the prediction of wall shear effects. In contrast, the stationary domain was meshed more coarsely away from the blade and deflector surfaces to reduce computational cost while maintaining sufficient accuracy in the main region of interest. As a result, this mesh configuration complements the selected solver setup by balancing numerical accuracy and computational efficiency, with priority given to resolving the complex flow phenomena around the SPHT blade.

3. Results and Discussion

3.1. Correlation of Water Flow Velocity to Mechanical Response

Bridging with the initial data, **Figure 9** illustrates the relationship between water-flow velocity (U), rotational speed (RPM), and tip-speed ratio (TSR) of the SPHT rotor. Generally, both RPM and TSR showed an increasing trend as the water-flow velocity increased. The rotor speed rose from 14 RPM at 0.50 m/s to 16 RPM at 0.62 m/s, then remained nearly constant around 16 RPM between 0.62 and 0.68 m/s, before increasing again to 17 RPM at 0.75 m/s and reaching 18 RPM at 0.83 m/s. This trend indicates that higher inlet velocity provided stronger hydrodynamic forcing on the blade surface, resulting in a higher rotational response. Although a brief plateau appeared in the mid-velocity region, the overall increase in RPM confirms that the rotor received greater driving torque as the flow of velocity increased.

Notably, the TSR profile followed a similar increasing tendency, indicating that the blade-tip response improved as the rotor speed increased under higher water-flow conditions. Since the rotor diameter was kept constant, the increase in TSR was mainly associated with the increase in rotational speed generated by stronger hydrodynamic loading. The similar RPM response observed for the two-blade and four-blade configurations suggests that blade number did not significantly alter the achievable rotational speed under the tested river velocities. Therefore, the main performance differences between the two configurations were expected to appear more clearly in torque generation, mechanical power, electrical output, and generator efficiency, rather than in rotational speed alone.

Building on the observed increase in rotor speed and TSR with water-flow velocity, **Figure 10** further compares how velocity influenced mechanical response, torque, and power for each blade configuration. For the two-blade rotor (see **Figure 10a**), both torque and power rose almost monotonically with increasing velocity, indicating a relatively smooth transfer of hydrodynamic forcing into shaft output; torque increased from 0.76 N.m at 0.50 m/s to 1.77 N.m near 0.83 m/s, while power escalated from 1.10 W to above 3.32 W over the same range. For the four-blade rotor (see **Figure 10b**), the same positive trend was observed but at consistently higher levels, with torque increasing from 1.79 N.m to 2.46 N.m and power arising from 2.61 W to around 4.62 W as velocity rises. Notably, the four-blade case depicted a sharper torque gain in the mid-velocity region (0.65–0.70 m/s), suggesting stronger flow engagement and higher effective solidity, which enhanced the driving moment under these conditions.

From these profiles, the four-blade configuration emerged as the optimum condition for maximizing mechanical output in this study, since the higher solidity of the blade delivers higher torque and higher power across the entire tested velocity range [29], including the highest recorded performance at the maximum velocity (0.83 m/s). It indicates that, under the present loading and river-flow conditions, the added blade solidity improved momentum capture and reduced the relative impact of negative torque on the returning side, resulting in superior self-starting capability compared to the two-blade rotor [30]. Consequently, for pico-scale generation, where dependable torque production has become critical for driving the stepper-generator under load, the four-blade SPHT arrangement was the preferred configuration.

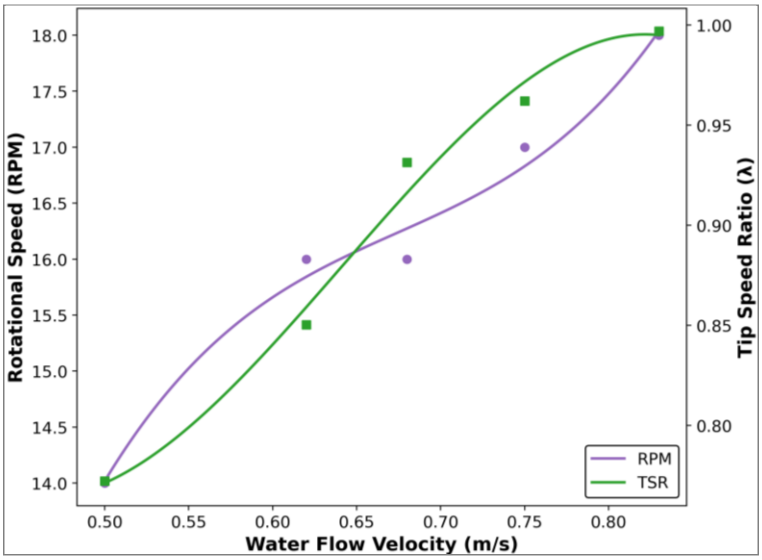

Figure 9. Water flow velocity profile toward the measured rotational speed

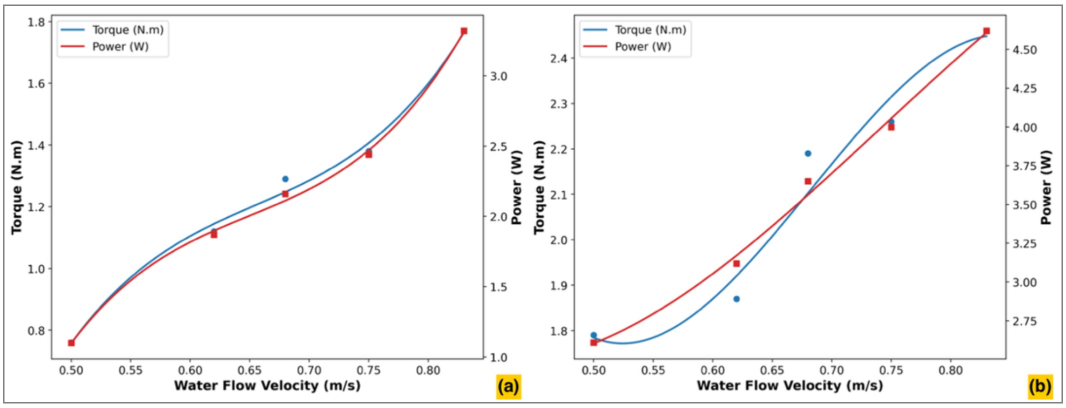

Figure 10. Correlation of velocity to mechanical response in different configurations: (a) Two-blades; (b) Four-blades

3.2. Connecting Tip-Speed-Ratio (TSR) toward Coefficient of Power (CP)

Building on the findings that both the two-blade and four-blade rotors produced essentially the same RPM and TSR under the tested river velocities, this subsection connected the tip-speed ratio (λ) to the coefficient of torque (CT) and the resulting coefficient of power (CP). **Figure 11** presents the performance profile in which CT and CP were plotted as functions of TSR. As λ increased from approximately 0.76 to 1.77, CP exhibited an overall rising trend, indicating improved conversion of the available flow power into useful mechanical output as the rotor approached higher operating TSR. Meanwhile, the CT curve escalated sharply at λ = 0.85, then slightly decreased toward λ = 0.92, reflecting a change in how effectively the rotor generated driving moment as the rotational condition shifted. Nonetheless, the continued increase of CP suggests that gains in rotational effectiveness and reduced relative losses dominated at higher TSR.

Based on **Figure 11**, the optimum operating condition within the tested range occurred near λ = 1.00, where the maximum CP (0.11) was obtained. It indicates that the SPHT system reached its highest conversion efficiency when operated close to this TSR, which could be achieved by appropriately matching the site velocity to the electrical or mechanical loading. Because TSR was observed to be comparable for both blade configurations, the optimum was primarily governed by the operating TSR rather than blade count. However, when paired with the earlier torque–power comparison (see **Figure 10**), the four-blade rotor remained the more advantageous configuration for delivering higher absolute output while operating near the same optimal TSR. Eventually, it was confirmed by Sakib & Griffith [31], who explained that increasing rotor solidity boosts the power coefficient.

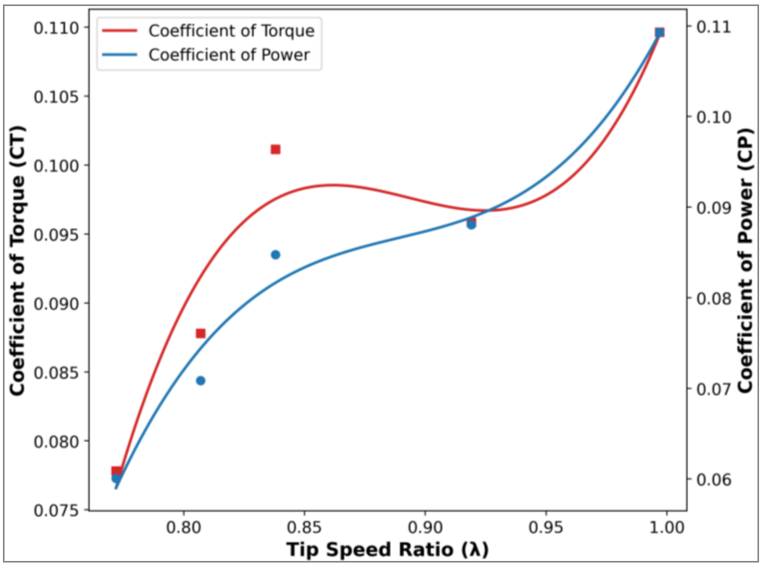

Figure 11. Profile of TSR toward CT to calculate CP for both blade configurations

3.3. Mechanical Performance Validation with Other Literatures

This subsection validates the mechanical performance of the proposed quarter-circular SPHT rotor by comparing its coefficient of power (Cp) and coefficient of torque (Ct) with selected Savonius-type turbine studies from the literature. The comparison is necessary because the present work introduces a quarter-circular blade profile, whereas most available studies still use conventional semi-circular or modified semi-circular blade geometries. Since direct benchmark data for quarter-circular SPHT rotors are still limited, the closest available Savonius turbine studies were used as comparative references. This approach allows the mechanical characteristics of the proposed rotor to be positioned more clearly within the broader development of Savonius pico-hydro and hydrokinetic turbines.

As shown in **Figure 12**, the mechanical performance of the present quarter-circular SPHT rotor is compared with several published Savonius-type turbine studies in terms of coefficient of power (Cp) and coefficient of torque (Ct). The comparison shows that the present rotor produced a lower Cp than Rehman *et al*. [32], Kumar *et al*. [33], and Rengma and Subbarao [34], particularly across the tested TSR range. A similar tendency was also observed in the Ct comparison, where the present rotor generated lower torque coefficient than those references. However, the present result remained comparable with El-Sawy *et al*. [35] and Patel *et al*. [36] at several TSR points, especially at higher TSR, where the Cp of the present rotor increased and approached or exceeded some of the lower literature curves. This indicates that the quarter-circular rotor was still able to convert flow energy into mechanical output, although its peak mechanical coefficient was generally lower than several previously reported Savonius configurations.

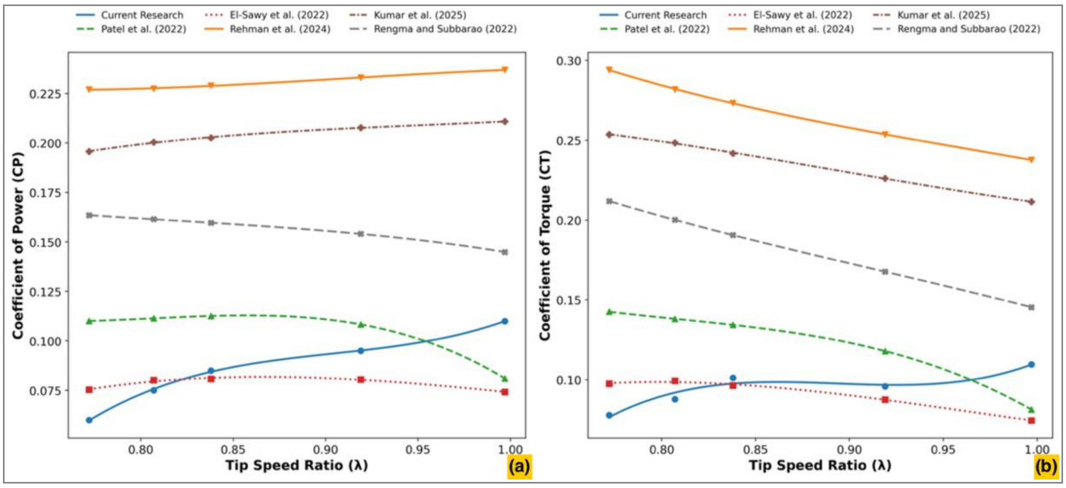

Figure 12. Comparison of TSR-CP curves between the current study (quarter circle) and previous findings (semi-circle); (a) Coefficient of power; (b) Coefficient of torque

The lower Cp and Ct values should not be interpreted as a failure of the present design. Instead, they provide an important mechanical validation of the proposed geometry. Most previous Savonius turbine studies used conventional semicircular blades or modified semicircular blade concepts, whereas this study adopts a quarter-circular blade profile, for which directly comparable reference data for quarter-circular SPHT rotors is still limited. Therefore, the present study was compared with the closest available semi-circular or modified Savonius turbine studies. Since the quarter-circular blade reduces the curved surface area and flow-capturing region compared with a conventional semi-circular blade, a reduction in pressure-driven torque and power coefficient is physically reasonable. The smaller concave surface may receive less hydrodynamic force [37], while the reduced projected blade area may limit the momentum exchange between the incoming flow and rotor surface.

This finding is academically important because lower comparative performance does not diminish the value of the research. In experimental fluid machinery studies, lower or unexpected results often provide useful evidence for understanding the effect of geometry on turbine behavior. In this case, the comparison suggests that reducing the conventional semi-circular Savonius blade into a quarter-circular profile tends to decrease the mechanical performance of the SPHT, particularly in terms of Cp and Ct. However, the proposed geometry still offers useful insight for compact rotor development, especially where space limitation, structural simplicity, manufacturability, or integration with electrical generation systems is considered. Therefore, the present comparison validates not only the performance level of the proposed rotor, but also the mechanical consequence of using a quarter-circular blade geometry.

Eventually, the literature comparison confirms that the quarter-circular SPHT rotor has a different performance characteristic from conventional semi-circular Savonius rotors. While the present rotor does not outperform the best reported configurations, it establishes a necessary baseline for quarter-circular blade performance in pico-hydro applications. This baseline is valuable because it clarifies that blade-surface reduction can lower mechanical output, while also providing a reference for future optimization through blade curvature refinement, overlap adjustment, deflector integration, and rotor solidity modification.

3.4. Interpreting Electrical Performance Records

While the previous subsection adopted TSR-based coefficients (CT and CP) to describe how effectively the SPHT converts the available flow into mechanical output, the system's practical value is ultimately determined by the electrical power it can deliver to a load. Accordingly, **Figure 13** summarizes the recorded generator response, including voltage (V), current (A), and electrical power (W), as functions of water-flow velocity for both blade configurations. Because the stepper motor was utilized as the generator, these electrical quantities reflected the combined effect of rotor dynamics, transmission or loading, and the generator's electromechanical characteristics, allowing the mechanical trends discussed earlier to be interpreted in terms of usable pico-scale energy production.

For the two-blade configuration (see **Figure 13a**), the output voltage escalated from 1 V at 0.50 m/s to 2 V at 0.62–0.68 m/s, then rose sharply to 4 V at 0.75 m/s, and reached 6 V at 0.83 m/s. In contrast, the current remained near 0 A up to 0.68 m/s, after which it increased markedly to about 0.4 A at 0.75 m/s and 0.5 A at 0.83 m/s, producing a corresponding jump in electrical power to roughly 1.2 W and 2.4 W, respectively. On the other hand, the four-blade configuration (see **Figure 13b**) exhibited stronger electrical response across the same velocity range: voltage increased from about 2 V (0.50 m/s) to 5 V (0.62 – 0.68 m/s), then to 6 V (0.75 m/s) and 8 V (0.83 m/s), with current rising from 0.3 A at mid-velocities to 0.5 A at the highest velocity. As a result, electrical power became substantial at moderate velocities (1.5 W at 0.62–0.68 m/s) and rose to 2.4 W at 0.75 m/s, reaching 3.9 W at 0.83 m/s, indicating that the higher-solidity rotor sustained stronger generator loading and more consistent energy conversion.

Based on these records, the optimum operating condition within the tested range occurred at the highest measured velocity, U = 0.83 m/s, where both configurations achieved their maximum electrical outputs; however, the four-blade rotor was clearly optimal overall because it delivered the highest voltage and power (8 V and 3.9 W) compared with the two-blade case (6 V and 2.4 W). Practically, it also suggests a more favorable operating regime for reliable generation at $U \geq 0.75$ m/s, where the electrical output became strongly responsive and stable under load, aligning with the earlier indication that performance improved as the system approached its upper TSR range. Furthermore, Memon *et al*. [38] confirmed that a slight increase in stress occurred as the number of blades increased to four.

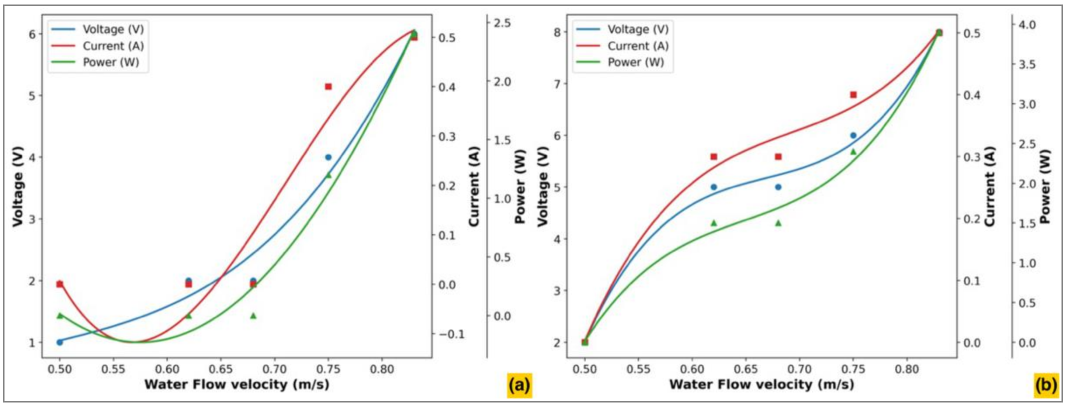

Figure 13. Generated electrical properties in each blade configuration: (a) Two-blades; (b) Four-blades

3.5. Measuring Generator Efficiency (%)

As a result, from the mechanical and electrical power in **Figure 10** and **Figure 13**, generator efficiency was evaluated by comparing the mechanical power delivered by the rotor to the electrical power produced by the stepper-generator over the tested water-flow velocities. Therefore, **Figure 14** summarizes these three quantities as a function of water velocity for each blade configuration, enabling direct interpretation of how effectively the SPHT–generator system converted hydrodynamic input into usable electrical output.

For the two-blade configuration (see **Figure 14a**), mechanical power rose steadily with velocity, whereas electrical power remained extremely small at the lower velocities and only rose noticeably at higher flow speeds. It exhibited a low-efficiency profile (and may appear unstable) in the low-velocity region. Once the flow reached the higher range, electrical power increased rapidly, and the efficiency climbed correspondingly, indicating that a larger fraction of the available mechanical power was converted into electrical output under stronger hydrodynamic forcing. Meanwhile, in the four-blade configuration (see **Figure 14b**), both powers were higher across the entire velocity range, and the efficiency grew more consistently toward the high-velocity condition. It reflects the greater torque-producing capability of the higher-solidity rotor, which improved generator loading and enabled stronger current generation at moderate velocities, not only near the maximum test point. The optimum operating condition in this dataset occurred at the highest tested velocity (0.83 m/s), where the system achieved its peak electrical output and highest efficiency. The overall comparison indicates that the four-blade SPHT was the preferred configuration for maximizing practical pico-scale generation efficiency under the tested river conditions.

These efficiency results confirmed that electrical conversion efficiency increased with water velocity, because higher hydrodynamic forcing raised shaft torque and speed sufficiently to overcome generator and circuit losses and sustain measurable current delivery. Under these conditions, the four-blade SPHT consistently provided higher mechanical input and electrical output as described by Eltayesh *et al*. [39], yielding a more stable and generally higher-efficiency trend than the two-blade rotor. The optimum operating point occurred at the maximum inlet condition (0.83 m/s), where electrical power and efficiency were highest, indicating that the four-blade configuration was the most suitable choice for practical pico-scale generation in the present setup.

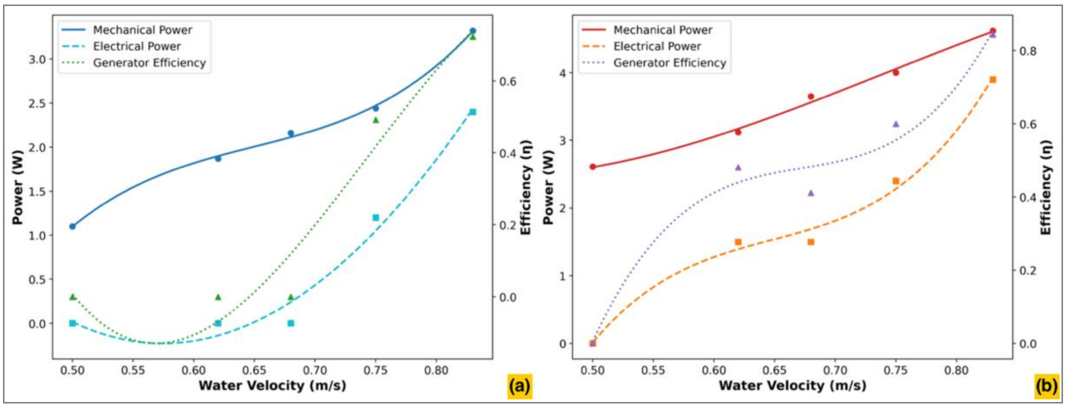

Figure 14. Electrical efficiency (%) in each blade configuration: (a) Two-blades; (b) Four-blades

3.6. Identifying Flow Behavior Through Numerical Simulation

To complement the field measurements and clarify the flow mechanisms responsible for the observed torque–power trends, the experimental study was extended through CFD analysis. Since the inlet velocity of 0.83 m/s produced better rotor performance than 0.50 m/s, the numerical comparison focused on this operating condition to evaluate the hydrodynamic differences between the two- and four-bladed SPHT configurations. Therefore, **Figure 15** presents the simulated velocity streamlines, velocity contours, and pressure contours for both blade configurations at U = 0.83 m/s. The results show that the four-blade configuration, which has higher solidity, produced a more continuous interaction between the incoming flow and the rotating blades. Compared with the two-blade rotor, the additional blade surfaces reduced low-velocity bypass flow through the rotor gap and increased the frequency of blade–flow interaction [40]. This condition strengthened momentum exchange between the water flow and the rotor, which is consistent with the higher torque obtained experimentally.

A closer examination of the CFD contours reveals that the main difference between the two rotor configurations lies in how each blade arrangement interacts with and redistributes the incoming flow. For the four-blade SPHT, the velocity field shows clearer high-velocity gradients around the blade tips and near the deflector, indicating stronger shear, local acceleration, recirculation, and wake development. In contrast, the two-blade rotor produced a more localized flow interaction region, suggesting that the smaller number of blade passages reduced the continuity of energy extraction from the incoming flow [41]. The broader and more distributed flow disturbance generated by the four-blade rotor allowed a larger portion of the flow to interact with the blade surfaces, thereby supporting higher mechanical and electrical output even when the TSR remained comparable.

This difference is also reflected in the pressure distribution around the rotor. In the two-blade configuration, the pressure field was more concentrated, with high-pressure regions mainly appearing on the upstream impingement side of the blade and low-pressure regions forming in the downstream recirculation area. Although this pressure difference contributed to tangential blade loading and torque generation, its effect was limited to fewer blade passages per revolution. By contrast, the four-blade rotor produced a more spatially distributed pressure pattern around the circumference, with stronger positive-pressure zones near the advancing blade sectors and broader low-pressure regions in the wake. This wider pressure distribution created a larger effective pressure difference acting across multiple blades, which improved the torque-producing capability of the rotor.

Surprisingly, the positive and negative pressure regions observed in the SPHT can be associated with local flow acceleration, recirculation, and vortex formation around the rotating blades and near the deflector [42]. As the flow passed through narrow blade passages and curved flow paths, the local velocity increased and the static pressure decreased, forming low-pressure zones due to the Bernoulli effect. The higher blade number also increased the surface area and complexity of the flow path, resulting in greater pressure variation around the rotor [43]. Furthermore, local flow separation and vortex structures near high-curvature blade regions contributed to the development of negative-pressure zones [44]. At U = 0.83 m/s, these effects became more pronounced because stronger shear and wall interaction caused greater pressure drops, recirculation intensity, and frictional losses around the blade surfaces [45], [46].

Eventually, the CFD results demonstrate that the superior performance of the four-blade SPHT at U = 0.83 m/s was mainly driven by stronger pressure gradients, more distributed blade loading, and improved momentum exchange between the flow and the rotor. The velocity and pressure contours therefore support the experimental findings, showing that the four-blade configuration enhanced torque generation and energy extraction more effectively than the two-blade rotor under the best-performing inlet condition [47].

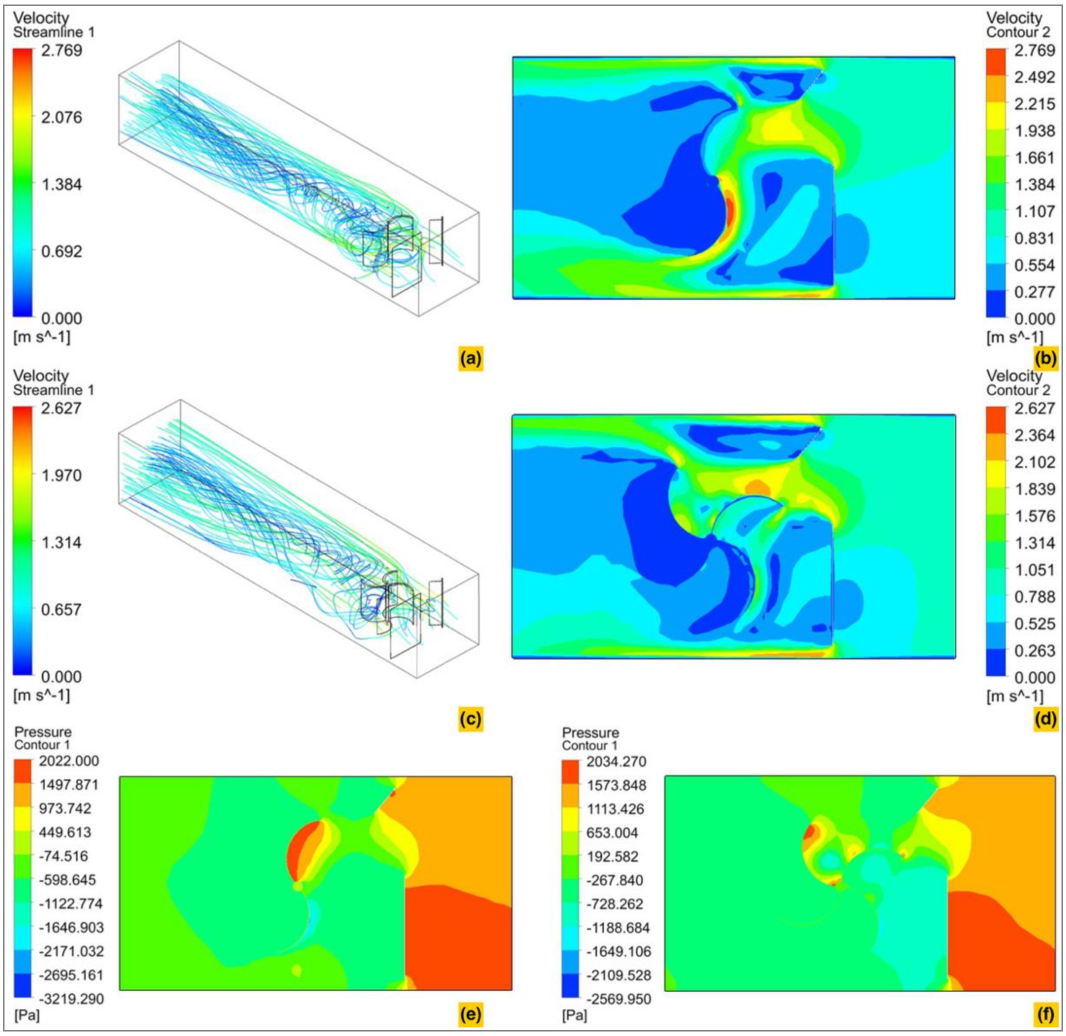

Figure 15. CFD comparison of flow characteristics for two- and four-bladed SPHT rotors at U = 0.83 m/s: (a) Velocity streamline of the two-blade rotor; (b) Velocity contour of the two-blade rotor; (c) Velocity streamline of the four-blade rotor; (d) Velocity contour of the four-blade rotor; (e) Pressure contour of the two-blade rotor; (f) Pressure contour of the four-blade rotor

3.7. Determining Optimum Deflector Angle to Enhance Mechanical Performance

After clarifying the influence of blade numbers on the velocity and pressure distributions, the analysis was extended to evaluate the effect of deflector angle, since the deflector governs the redirection of incoming flow momentum toward the advancing blade. In the SPHT system, the deflector serves both as a shielding component for the returning blade side and as a flow-guiding element that directs the incoming stream toward the concave driving surface. Consequently, variations in deflector orientation can alter the local acceleration field, pressure distribution, recirculation pattern, wake development, and pressure-drop characteristics around the rotor. In this study, the pressure drop was quantified numerically from the CFD simulation rather than obtained through direct experimental measurement. **Figure 16** presents the simulated pressure and velocity contours of the four-bladed SPHT rotor at deflector angles of 20°, 30°, 40°, and 50°.

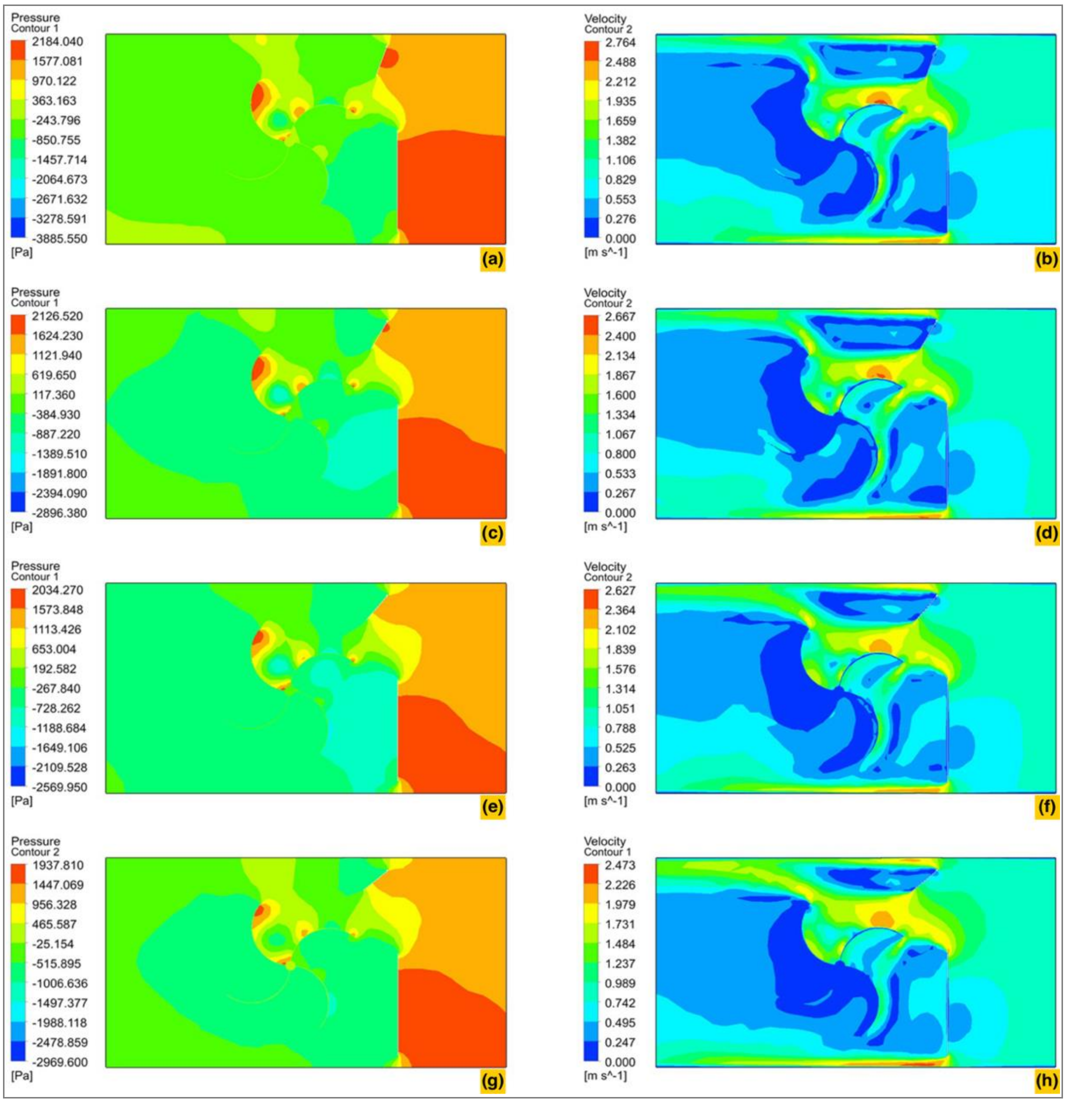

Figure 16. Effect of deflector angle on the CFD pressure and velocity fields of the four-bladed SPHT rotor: pressure and velocity contours at: (a, b) 20°; (c, d) 30°; (e, f) 40°; (g, h) 50° deflector angles

These contours indicate that the deflector angle strongly affected the balance between flow guidance, blockage behind the deflector, and vortex formation around the rotor. At 20°, the deflector produced the strongest guiding effect by directing the incoming flow toward the rotor passage. However, this condition also generated a relatively high blockage effect behind the deflector, which increased profile loss and reduced the overall flow efficiency. Therefore, although the 20° case showed strong flow redirection, it was not considered as the optimum condition because the benefit of its guiding effect was partly offset by the higher blockage loss behind the deflector.

At 30°, the guiding effect remained relatively comparable to the 20° case, as shown by the clear flow passage toward the advancing blade and the absence of strong vortex formation around the rotor. More importantly, the blockage effect behind the deflector was slightly lower than that observed at 20°, producing a better compromise between effective flow guidance and acceptable profile loss. This condition allowed the incoming flow to reach the rotor more smoothly while maintaining sufficient momentum transfer to the blade. As illustrated in **Figure 17b**, the velocity contour at 30° shows a clear flow channel without vortex disturbance, indicating that the rotor passage was more stable and better aligned with the incoming stream.

For higher deflector angles, particularly 40° and 50°, the blockage effect behind the deflector became weaker, with the 50° case showing the lowest blockage tendency. However, this reduction did not improve the overall flow performance because the dominant loss mechanism shifted to vortex formation around the rotor. In these cases, the flow passage became less clear, and stronger vortical structures developed around the blade interaction region. These vortices caused a significant pressure drop (see **Figure 17a**) and disrupted effective momentum transfer toward the advancing blade, making the flow less efficient despite the lower blockage behind the deflector. Thus, increasing the deflector angle beyond 30° did not provide a hydrodynamic advantage because the reduction in blockage loss was outweighed by vortex-induced pressure losses around the rotor. For this reason, the 30° deflector angle was selected as the best configuration for improving the hydrodynamic performance of the four-bladed SPHT system.

Since the experimental turbine in this study was operated using a 30° deflector angle, these CFD results provide supporting evidence that the experimental setup was tested under the most balanced and favorable deflector condition. Therefore, the selected 30° angle was not only a design choice, but also a condition validated by the pressure-drop behavior and flow-field structure, indicating that the experimental performance was obtained under the best deflector configuration for the present SPHT system.

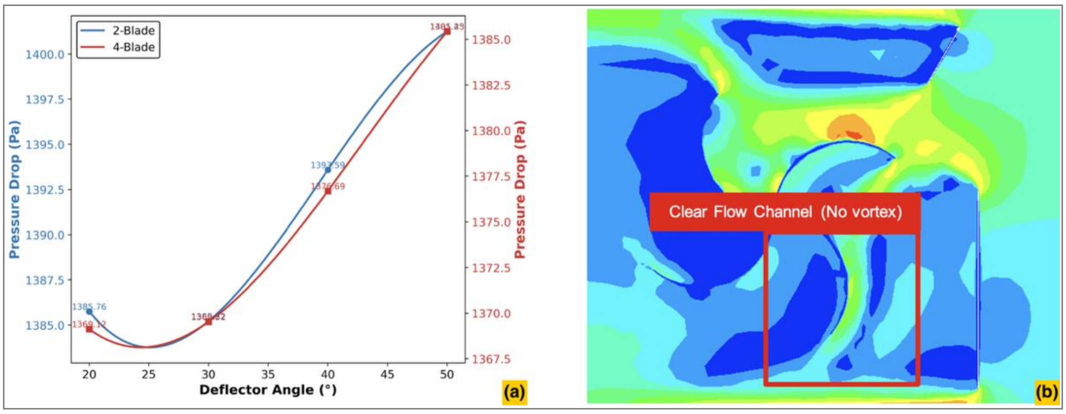

Figure 17. (a) Numerically obtained pressure-drop comparison between the two- and four-bladed SPHT rotors at different deflector angles; (b) Velocity contour at the 30° deflector angle, indicating a well-defined flow passage with reduced vortex formation around the rotor

4. Conclusion

This study evaluated the performance of a Savonius Pico-Hydro Turbine (SPHT) through experimental testing and CFD simulation. The analysis focused on the effects of blade number and deflector angle on mechanical response, electrical output, and flow behavior. A limitation of this study is that the deflector-angle comparison was conducted numerically using CFD, while the experiment used only the selected 30° deflector angle. Therefore, future work should experimentally test different deflector angles, especially for pico-hydro turbine generator applications. Future studies should also include error and uncertainty analysis, transient CFD simulation, generator-load optimization, and long-term field testing under variable flow conditions. Eventually, the main conclusions are as follows:

a. The novelty of this study is the development and evaluation of an SPHT rotor with a quarter-circular blade profile, instead of the commonly used semi-circular Savonius blade. This design was assessed using mechanical and electrical experiments supported by CFD analysis.
b. The four-blade SPHT performed better than the two-blade SPHT. It produced higher torque and more stable electrical output because the additional blades improved flow interaction and momentum transfer to the rotor.
c. The CFD results confirmed the experimental trends. The four-blade rotor produced a more distributed velocity and pressure field, stronger pressure loading, and clearer flow interaction around the rotor, which explains its higher torque-producing capability.
d. A deflector angle of 30° was identified as the best condition in this study. This angle provides a clear flow path with reduced vortex formation and a good balance between flow guidance and pressure loss, showing promising potential for pico-scale hydropower applications.

Acknowledgements

The authors express their sincere gratitude to the volunteers from the Department of Mechanical Technology at Universitas Muhammadiyah Yogyakarta, Nova Triwono and Muhammad

Nurhudha Lathif, for their valuable contributions to this research. Their dedication to fieldwork, data collection, and experimental validation significantly strengthened the quality of this study. The authors also gratefully acknowledge PT Sahla Inovatif Teknik (Yogyakarta, Indonesia) for its valuable support as an industrial partner, including facilitating access to simulation resources and technical assistance.

Authors' Declaration

Authors' contributions and responsibilities – R.A.A.: Conceptualization, project administration, data preparation, methodology, writing-reviewing and editing; S.S.: Frame manufacturing, supervision, and apparatus experimental setting; Y.B.: Data visualization, methodology, writing-original draft; M.Y.I.: Blade manufacturing and computational simulation.

Funding – This research was funded by Universitas Muhammadiyah Yogyakarta through the Internal Research Grant Program under Contract Number: 16/R-LRI/I/2023 and Muhammadiyah National Research Grant Program under Contract Number: 0258.936/I.3/D/2025.

Availability of data and materials – All data is available from the authors.

Competing interests – The authors declare no competing interests.

Generative AI statement - The authors used ChatGPT to help brainstorm the initial outline and structure of the manuscript introduction and grapichal abstract. Whereas, the experimental data, numerical simulations, data analysis, interpretation, and conclusions presented in this manuscript were entirely produced and verified by the authors. The authors critically reviewed, verified, and substantially revised the generated output, and assume full responsibility for the final integrity of this research.

Additional information – No additional information from the authors.

References

[1] International Energy Agency, "Electricity – Global Energy Review 2025 – Analysis," International Energy Agency. Accessed: Dec. 13, 2025. [Online]. Available: https://www.iea.org/reports/global-energy-review-2025/electricity

[2] Seetharaman, K. Moorthy, N. Patwa, Saravanan, and Y. Gupta, "Breaking barriers in deployment of renewable energy," *Heliyon*, vol. 5, no. 1, p. e01166, Jan. 2019, doi: 10.1016/j.heliyon.2019.e01166.

[3] D. Mhlanga and E. Ndhlovu, "The Russia Ukraine War, Global Energy Supply, and Sustainable Development," in *Contributions to Political Science*, 2024, pp. 263–280. doi: 10.1007/978-3-031-63333-1_16.

[4] Y. Budiman and A. Khoirunnisa', "Predictive analysis of biofuel production in prominent Asian markets: Implications for renewable energy development (2045-2050)," *IOP Conference Series: Earth and Environmental Science*, vol. 1518, no. 1, p. 012009, Jun. 2025, doi: 10.1088/1755-1315/1518/1/012009.

[5] R. Thomas *et al.*, "Land instability Compounds the risk of sea level rise in Alexandria, Egypt," *International Journal of Applied Earth Observation and Geoinformation*, vol. 141, p. 104648, Jul. 2025, doi: 10.1016/j.jag.2025.104648.

[6] U. A. Bhatti *et al.*, "Global production patterns: Understanding the relationship between greenhouse gas emissions, agriculture greening and climate variability," *Environmental Research*, vol. 245, p. 118049, Mar. 2024, doi: 10.1016/j.envres.2023.118049.

[7] K. R. Shivanna, "Climate change and its impact on biodiversity and human welfare," *Proceedings of the Indian National Science Academy*, vol. 88, no. 2, pp. 160–171, Jun. 2022, doi: 10.1007/s43538-022-00073-6.

[8] M. Taušová, M. Mykhei, K. Čulková, and P. Tauš, "Comparison of Renewable Energy Implementation in Geographically and Climatically Diverse Regions," *Sustainability*, vol. 17, no. 7, p. 3098, Mar. 2025, doi: 10.3390/su17073098.

[9] Å. Killingtveit, "Hydroelectric Power," in *Future Energy*, Elsevier, 2020, pp. 315–330. doi: 10.1016/B978-0-08-102886-5.00015-3.

[10] L. S. Paraschiv and S. Paraschiv, "Contribution of renewable energy (hydro, wind, solar and biomass) to decarbonization and transformation of the electricity generation sector for sustainable development," *Energy Reports*, vol. 9, pp. 535–544, Sep. 2023, doi: 10.1016/j.egyr.2023.07.024.

[11] Muhd Syukri Mohd Shamsuddin, Nujjiya Abdul Mu'in, and Noorfazreena Mohammad Kamaruddin, "Experimental Investigation of the Savonius Turbine for Low-Speed Hydrokinetic Applications in Small Rivers," *Journal of Advanced Research in Fluid Mechanics and Thermal Sciences*, vol. 94, no. 2, pp. 29–46, May 2022, doi: 10.37934/arfmts.94.2.2946.

[12] K. C. Sarma, B. Nath, A. Biswas, and R. D. Misra, "Design and performance investigation of a triple blade dual stage Savonius-alike hydrokinetic turbine from low flow stream reserves," *Energy Sources, Part A: Recovery, Utilization, and Environmental Effects*, vol. 45, no. 4, pp. 12099–12117, Oct. 2023, doi: 10.1080/15567036.2023.2268572.

[13] M. Basumatary and A. Biswas, "Numerical simulation of two-bladed Savonius water turbine with deflector," *International Journal of Renewable Energy Technology*, vol. 7, no. 4, p. 383, 2016, doi: 10.1504/IJRET.2016.080115.

[14] B. Nath, A. Biswas, B. Das, and R. Dev Misra, "Design, optimization and analysis of a modified Savonius hydro-kinetic turbine (MSHT) with curved winglet and straight blade," *Energy Conversion and Management*, vol. 314, p. 118699, Aug. 2024, doi: 10.1016/j.enconman.2024.118699.

[15] R. A. Anugrah, F. Yuafiq, M. Yusuf, M. H. Bin Peeie, and A. Yudianto, "Computational Fluid Dynamics of Savonius Water Turbine for Hydrokinetic Pico Hydro Systems," *BIO Web of Conferences*, vol. 199, p. 02009, Dec. 2025, doi: 10.1051/bioconf/202519902009.

[16] E. Cuce and P. M. Cuce, "Approach of the solar chimney power plants by computational fluid dynamics (CFD)," in *Solar Chimney Power Plants*, Elsevier, 2025, pp. 139–170. doi: 10.1016/B978-0-443-24816-0.00007-3.

[17] R. A. Anugrah, "Design of HAWT with solar panel for hybrid power plant," in *AIP Conference Proceedings*, Aug. 2025, p. 090008. doi: 10.1063/5.0259874.

[18] G. R. Hübner, H. Pinheiro, C. E. de Souza, C. M. Franchi, L. D. da Rosa, and J. P. Dias, "Detection of mass imbalance in the rotor of wind turbines using Support Vector Machine," *Renewable Energy*, vol. 170, pp. 49–59, Jun. 2021, doi: 10.1016/j.renene.2021.01.080.

[19] Z. Zhao *et al.*, "Effect of blade and tower interference on wind turbine tower vibration occurred before grid connection," *Sustainable Energy Technologies and Assessments*, vol. 76, p. 104290, Apr. 2025, doi: 10.1016/j.seta.2025.104290.

[20] M. Badrul Salleh, N. M. Kamaruddin, and Z. Mohamed-Kassim, "Savonius hydrokinetic turbines for a sustainable river-based energy extraction: A review of the technology and potential applications in Malaysia," *Sustainable Energy Technologies and Assessments*, vol. 36, p. 100554, Dec. 2019, doi: 10.1016/j.seta.2019.100554.

[21] E. Fatahian, F. Ismail, M. H. H. Ishak, and W. S. Chang, "Aerodynamic performance improvement of Savonius wind turbine through a passive flow control method using grooved surfaces on a deflector," *Ocean Engineering*, vol. 284, p. 115282, Sep. 2023, doi: 10.1016/j.oceaneng.2023.115282.

[22] Muhammad Mizan, Warjito, Budiarso, Ridho Irwansyah, Muhamad Agil Fadhel Kurnianto, and Muhammad Faridz Athaya, "The Performance of the Pico Scale Turgo Water Turbine Coconut Shell Blade with Variations in Nozzle Diameter and Distance," *Journal of Advanced Research in Fluid Mechanics and Thermal Sciences*, vol. 100, no. 1, pp. 53–62, Dec. 2022, doi: 10.37934/arfmts.100.1.5362.

[23] R. A. Anugrah, Y. Budiman, A. Widyianto, A. Hadi, H. S. Novanto, and A. Yudianto, "Novel construction of hybrid wind turbine with solar panels: A comprehensive analysis through experimental study and numerical simulation," *Cleaner Energy Systems*, vol. 13, p. 100242, Jun. 2026, doi: 10.1016/j.cles.2026.100242.

[24] I. Safdar, S. Sultan, H. A. Raza, M. Umer, and M. Ali, "Empirical analysis of turbine and generator efficiency of a pico hydro system," *Sustainable Energy Technologies and Assessments*, vol. 37, p. 100605, Feb. 2020, doi: 10.1016/j.seta.2019.100605.

[25] Kaprawi Sahim *et al.*, "Experimental Study of Darrieus Water Turbine Two Blade Different Configuration and Hybrid Turbine for Application of an Irrigation Flow," *Journal of Advanced Research in Fluid Mechanics and Thermal Sciences*, vol. 98, no. 2, pp. 58–66, Sep. 2022, doi:

10.37934/arfmts.98.2.5866.

[26] R. A. Anugrah and S. Muzamil, “Development of Real-Time Data Acquisition Device for Monitoring Torque and RPM of Picohydro-Scale Savonius Water Turbine,” in *2025 5th International Conference on Electronic and Electrical Engineering and Intelligent System (ICE3IS)*, IEEE, Aug. 2025, pp. 113–118. doi: 10.1109/ICE3IS66769.2025.11280876.

[27] R. A. Anugrah *et al.*, “Experimental Study and Computational Fluid Dynamics Simulation of Savonius Wind Turbines Using L-shaped Composite Blades for Low-wind Speed,” *Journal of Applied Fluid Mechanics*, vol. 19, no. 7, pp. 1593–1612, Jul. 2026, doi: 10.47176/jafm.19.7.4141.

[28] R. A. Anugrah, Y. Budiman, and M. H. Bin Peeie, “Performance and durability evaluation of a catamaran-based flood depth detection system using experiments and hydrodynamic simulations,” *Journal of Engineering Research*, Apr. 2026, doi: 10.1016/j.jer.2026.04.031.

[29] M. Kulak, M. Lipian, K. Olasek, M. Pereira, and F. Ravelet, “Rotor solidity and blade pitch influence on horizontal axis small wind turbine performance – Experimental study,” *Energy Reports*, vol. 12, pp. 4568–4577, Dec. 2024, doi: 10.1016/j.egyr.2024.10.036.

[30] A. Abdolahifar and A. Zanj, “A review of available solutions for enhancing aerodynamic performance in Darrieus vertical-axis wind turbines: A comparative discussion,” *Energy Conversion and Management*, vol. 327, p. 119575, Mar. 2025, doi: 10.1016/j.enconman.2025.119575.

[31] M. S. Sakib and D. T. Griffith, “Parked and operating load analysis in the aerodynamic design of multi-megawatt-scale floating vertical-axis wind turbines,” *Wind Energy Science*, vol. 7, no. 2, pp. 677–696, Mar. 2022, doi: 10.5194/wes-7-677-2022.

[32] M. U. Rehman and Z. Ali, “Performance improvement of Savonius hydrokinetic turbine using upstream crescent shape deflector,” *Multiscale and Multidisciplinary Modeling, Experiments and Design*, vol. 8, no. 1, p. 3, Jan. 2025, doi: 10.1007/s41939-024-00598-x.

[33] R. Kumar, A. Kumar, A. K. Shukla, U. M. R. Paturi, and M. Shabeeh, “Impact of Slot Shapes on the Savonius Hydrokinetic Turbine Performance,” in *Lecture Notes in Mechanical Engineering*, 2026, pp. 155–167. doi: 10.1007/978-981-96-7480-0_12.

[34] T. S. A. Rengma and P. M. V. B. Subbarao, “Water Flow Velocity Driven Modified Savonius Hydrokinetic Turbine,” *International Journal of Mechanical Engineering and Robotics Research*, vol. 11, no. 5, pp. 296–303, May 2022, doi: 10.18178/ijmerr.11.5.296-303.

[35] M. El-Sawy, A. S. Shehata, A. . A. Elbatran, and A. Tawfiq, “Numerical simulation of flow in hydrokinetic turbine channel to improve its efficiency by using first and second-law efficiency analysis,” *Ocean Engineering*, vol. 244, p. 110400, Jan. 2022, doi: 10.1016/j.oceaneng.2021.110400.

[36] R. Patel and V. Patel, “Performance analysis of Savonius hydrokinetic turbine using ‘C’ shaped Deflector,” *Energy Sources, Part A: Recovery, Utilization, and Environmental Effects*, vol. 44, no. 3, pp. 6618–6631, Sep. 2022, doi: 10.1080/15567036.2022.2101718.

[37] M. R. Ahmed, M. Faizal, and Y.-H. Lee, “Optimization of blade curvature and inter-rotor spacing of Savonius rotors for maximum wave energy extraction,” *Ocean Engineering*, vol. 65, pp. 32–38, Jun. 2013, doi: 10.1016/j.oceaneng.2013.02.005.

[38] Z. A. Memon, A. A. Sahito, Z. H. Leghari, P. H. Shaikh, and P. H. Shaikh, “Output Voltage Characteristics of Wind Energy System Considering Wind Speed and Number of Blades,” 2016.

[39] A. Eltayesh *et al.*, “Experimental and numerical investigation of the effect of blade number on the aerodynamic performance of a small-scale horizontal axis wind turbine,” *Alexandria Engineering Journal*, vol. 60, no. 4, pp. 3931–3944, Aug. 2021, doi: 10.1016/j.aej.2021.02.048.

[40] A. Sajedin, J. Allport, M. Amoozgar, and O. F. Marandi, “Blade thickness effects on viscous flutter in a radial turbocharger turbine,” *Engineering Failure Analysis*, vol. 136, p. 106139, Jun. 2022, doi: 10.1016/j.engfailanal.2022.106139.

[41] E. Y. Assefa and A. H. Tesfay, “Synergetic Improvement of Blade Entry and Water Admission Angles for High Efficiency Cross-Flow Turbines in Micro-Hydropower Applications,” *Energies*, vol. 18, no. 17, p. 4540, Aug. 2025, doi: 10.3390/en18174540.

[42] Z. Li, Y. Yuan, B. Guo, V. L. Varsegov, and J. Yao, “The Recirculation Zone Characteristics of the Circular Transverse Jet in Crossflow,” *Energies*, vol. 13, no. 12, p. 3224, Jun. 2020, doi: 10.3390/en13123224.

[43] Thoharudin, T. Santosa, H. Irawan, and H. Waloyo, “Investigation of Blade Number Effect on the Centrifugal Blower as a Small-Scale Water Turbine,” *Journal of Physics: Conference Series*, vol. 2989, no. 1, p. 012008, Apr. 2025, doi: 10.1088/1742-6596/2989/1/012008.

[44] X. Li *et al.*, “Aeroelastic instability of ultra-long flexible blades in floating offshore wind turbines: A state-of-the-art review,” *Advances in Wind Engineering*, vol. 3, no. 3, p. 100123, Sep. 2026, doi: 10.1016/j.awe.2026.100123.

[45] J. Huo, W. Zhang, J. Zhang, and L. Wang, “Flow dynamics characteristics of cleaning aircraft engine compressor blades using air-water mist flow,” *AIP Advances*, vol. 15, no. 12, Dec. 2025, doi: 10.1063/5.0300955.

[46] G. R. H. Abo Elyamin, M. A. Bassily, K. Y. Khalil, and M. S. Gomaa, “Effect of impeller blades number on the performance of a centrifugal pump,” *Alexandria Engineering Journal*, vol. 58, no. 1, pp. 39–48, Mar. 2019, doi: 10.1016/j.aej.2019.02.004.

[47] Zamzami, A. Akhyar, S. E. Sofyan, Suriadi, and Khairil, “A review of vortex water turbine design for sustainable energy generation (principles, optimization, and validation),” *Energy Conversion and Management: X*, vol. 26, p. 100895, Apr. 2025, doi: 10.1016/j.ecmx.2025.100895.